Thermal-annealing effects on the structural and magnetic properties of 10% Fe-doped SnO_2 nanoparticles synthetized by a polymer precursor method

F.H. Aragón [a,b,*], J.A.H. Coaquira [a], L.C.C.M. Nagamine [c], R. Cohen [c], S.W. da Silva [a,b], P.C. Morais [a,d]

[a] Núcleo de Física Aplicada, Instituto de Física, Universidade de Brasília, Brasília DF 70910-900, Brazil
[b] Instituto de Ciências Biológicas, Pós-graduação em Nanociência e Nanobiotecnologia, Universidade de Brasília, Brasilia DF 70919-970, Brazil
[c] Instituto de Física, Universidade de São Paulo, São Paulo SP 05508-090, Brazil
[d] Huazhong University of Science and Technology, School of Automation, Wuhan 430074, China

ARTICLE INFO

ABSTRACT

In this work, we present the experimental results of $Sn_{0.9}Fe_{0.1}O_2$ nanoparticles synthesized by a polymer precursor method. Studies were performed in the as-prepared (AP) and thermally-annealed (TA) samples. The X-ray diffraction (XRD) data analysis carried out using the Rietveld refinement method shows the formation of only the rutile-type structure in the AP sample and this phase remains stable for the TA sample. Additionally, the mean crystallite size shows an increase from ~ 4 nm to ~ 17 nm after the annealing and a clear reduction of the residual strain has also been determined. Micro-Raman spectroscopy measurements show the formation of an iron oxide phase (likely $\alpha\text{-}Fe_2O_3$) after the thermal treatment. Magnetic measurements show a paramagnetic behavior for the AP sample and the coexistence of a weak ferromagnetism and paramagnetism for the TA sample. The magnetically-ordered contribution of the TA sample has been assigned to the formation of the hematite phase. DC and AC magnetic features of the TA sample are consistent with a cluster-glass behavior which seems to be related to the magnetic disorder of spins located at the particle surface. Those spins clusters seem to be formed due to the diffusion of iron ions from the core of the particle to the surface caused by the annealing process.

© 2014 Elsevier B.V. All rights reserved.

1. Introduction

The possibility of using the magnetic properties of gas sensing materials instead of their conventional electrical properties has increased the interest in nanosized dilute magnetic semiconductor oxides [1]. This is because, meanwhile conventional gas sensors based on nanopowder systems face challenges in making good electrical contacts and obtaining accurate results from the electrical response, the monitoring of the magnetic response of nanostructured gas sensing materials avoids the need for electrical contacts, therefore simplifying the manufacture of devices [2].

Tin dioxide (SnO_2) is a wide band-gap (~ 3.5 eV) semiconductor and widely studied due to its potential applications as conventional gas sensor due to its high reactivity with environmental gases [3], catalyst for hydrocarbons oxidation [4],

transparent electrodes [5], and so forth. Through the doping of SnO_2 with transition metals (TM) to produce the known oxide-diluted magnetic semiconductor (ODMS), it is expected changes in its sensitivity, selectivity, and time response with respect to a number of pollutant gases. This effect can be observed by measuring the electrical response of TM-doped SnO_2 to a gas flow [6]. However, a pollutant gas can be also sensed by monitoring the changes in the magnetization of an ODMS system produced by a specific flow of that gas [1,2]. In order to use these ODMS systems as a magnetic gas sensing materials, they need to show ferromagnetic properties above room temperature. Punnoose et al. [7] has reported room-temperature ferromagnetism (FM) for the chemically synthesized $Sn_{1-x}Fe_xO_2$ powders. However, that FM disappears after a thermal annealing at temperatures above 600 °C. The latter result is in agreement with that reported by Mathew et al. [8]. This disappearance has been assigned to the expulsion of Fe from substitutional sites of the SnO_2 lattice. Moreover, Fe-doped SnO_2 nanoparticles (with Fe content below $< 5\%$) synthetized by a

coprecipitation method showed antiferromagnetic behavior [9]. More recently, room-temperature FM has been reported for Fe and Ni co-doped nanoparticles synthetized by a sol–gel method [10]. In order to shed some light on this issue, the effect of the thermal annealing on the structural and magnetic properties of Fe-doped SnO_2 nanoparticles is presented in this work.

## 2. Experimental details

SnO_2 nanoparticles doped with 10% Fe have been synthesized by a polymeric precursor method. The liquid precursor of Fe-doped SnO_2 was obtained by mixing tin citrate ($Sn_2(C_6O_7H_4) \cdot H_2O$), prepared from $SnCl_2 \cdot 2H_2O$ and the Fe precursor (Fe $(NO_3)_3 \cdot 9H_2O$), using a nominal proportion. At the thermal decomposition stage, the resultant product was firstly calcinated at 400 °C for 4 h and, after grinding in an agate mortar, an additional calcination at 400 °C to 4 h has been done in order to warrant the phase formation. Further preparation details are reported elsewhere [11]. The thermally-annealed (TA) sample has been obtained by annealing the as-prepared one at 900 °C for 2 h in air atmosphere. The crystal quality and average crystallite size were determined from X-ray powder diffraction (XRD) data obtained by using a commercial diffractometer with a Cu K_α radiation source. The XRD patterns were refined by using the Rietveld refinement method (via the DBWS program). The high resolution transmission electron microscopy (HRTEM) images were acquired in a JEOL JEN-2100 electron microscopy. Micro-Raman measurements were performed using a commercial triple spectrometer (Jobin Yvon, T64000), the sample was excited by the 514 nm line of a Ar^+-laser beam and detected with a liquid-nitrogen-cooled charge-coupled device. Room temperature micro-Raman spectra of powder samples were obtained in the range from 200 to 850 cm^{-1}. AC and DC magnetic measurements were performed in a physical property measurement system, PPMS (Quantum Design). Those measurements were carried out in the temperature range from 5 to 300 K and applying magnetic fields up to ± 90 kOe. The AC excitation field frequencies were in the range from 133 to 9333 Hz.

3. Results and discussion

3.1. Structural characterization

Fig. 1(a) shows the XRD pattern of the as-prepared (AP) and TA 10% Fe-doped SnO_2 samples. The formation of the tetragonal rutile-type crystal structure (space group $P4_2$/mnm) has been determined for both samples. A list of the structural parameters obtained from the refinement is presented in Table 1. No extra Bragg reflections have been observed in both patterns, which exclude the occurrence of additional crystalline phases within the resolution limit. As observed in Fig. 1, the linewidth of the Bragg reflections becomes narrower after the thermal treatment and the background signal become less intense. Meanwhile, the latter must be related to the crystallization of likely amorphous regions, the peak narrowing must be related to both the crystallite size growth and stress reduction. In order to estimate the mean crystallite size and the residual strain, the linewidth of the Bragg reflections have been used. During the Rietveld refinement, the peak shape was modeled using the Thompson-Cox-Hastings pseudo-Voight function (TCH-pV) [12,13]. The line broadening related to the instrumental contribution was corrected by adequately subtracting the linewidth of a standard sample (Si single crystal) from the linewidth of the studied sample. Assuming that the final linewidth (β) is only related to the crystallite size and residual strain, the following relation can be used to evaluate both
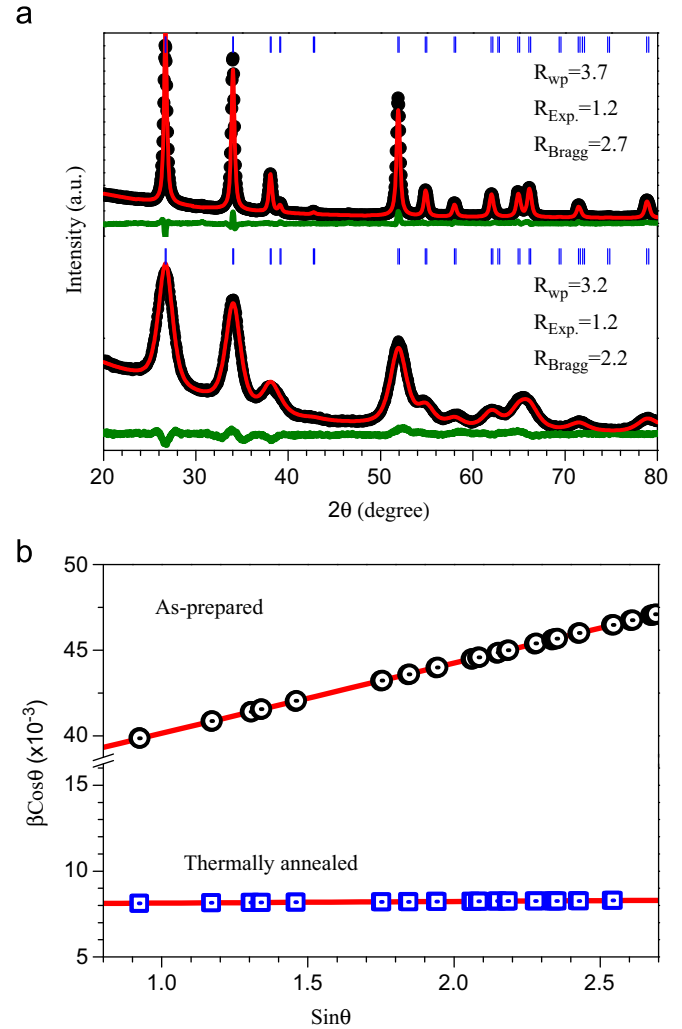
Fig. 1. (a) Room temperature XRD patterns of 10% Fe-doped SnO_2 nanoparticles. The bottom part corresponds to the AP sample and the upper part to the TA sample. The observed and calculated data are represented by the points and solid line, respectively. Parameters which represent the refinement quality are also included. The solid line at the bottom represents the difference between the observed and calculated data. (b) Williamson–Hall plots of both samples which are used to estimate the mean crystallite size and the residual strain

parameters:

$$\beta \cos \theta = K\lambda/\langle D \rangle + 4\varepsilon \sin \theta \qquad (1)$$

where $\langle D \rangle$ is the mean crystallite size, ε is the residual strain and K is a dimensionless factor that depends on the particle shape ($K \sim 0.9$ for a spherical shape). If one plots $\beta \cos \theta$ as a function of $\sin \theta$ (the Williamson–Hall plot), $\langle D \rangle$ and ε can be estimated from the linear fit. The obtained values are presented in Table 1.

As observed in Table 1, the lattice constants of the as-prepared 10% Fe-doped SnO_2 nanoparticles are smaller than those ones obtained for the undoped SnO_2 nanoparticles or SnO_2 bulk. It implies that the entrance of iron ions into the matrix leads to the substitution of Sn^{4+} ions by Fe^{3+} ions, since Sn^{4+} ions are larger than Fe^{3+} ions ($Fe^{3+} = 0.64$ Å, $Sn^{4+} = 0.71$ Å). In order to keep the charge neutrality of the system some defects such as oxygen vacancies are expected to be formed as a result of the doping process. After the annealing, the lattice constants show an asymmetric increase ($\Delta a/a \sim 0.05\%$ and $\Delta c/c \sim 0.10\%$). These changes drive to the increase of the unit cell volume of $\Delta V/V \sim 0.21\%$. These changes have been assigned to the out diffusion of the iron ions

Table 1
List of parameters obtained from the Rietveld refinement of the XRD patterns of 10% Fe-doped SnO_2 nanoparticles. The numbers between parentheses represent the uncertainties.

| Sample	a (Å)	c (Å)	u	Volume (Å³)	$\langle D \rangle_{TEM}$ (nm)	$\langle D \rangle_{XRD}$ (nm)	Strain (%)
AP	4.7332(1)	3.1796(1)	0.3013(1)	71.233(5)	–	4(1)	0.102
TA	4.7358(1)	3.1827(1)	0.3034(1)	71.381(5)	18(2)	17(1)	0.002
SnO_2[a]	4.7371	3.1866	0.3094	71.508	–	11(1)	0.205
SnO_2 (bulk)[b]	4.7380	3.1865	0.3071	71.533	–	–	–

[a] Parameters of undoped SnO_2 nanoparticles taken from Ref. [16].
[b] Parameters of bulk SnO_2 taken from Ref. [17].

from the SnO_2 matrix, likely through the channels of the rutile structure. This result is consistent with works reported in the literature [7,8]. On the other hand, the residual strain is drastically reduced in the thermally annealed sample. If this strain is originated at the particle surface, then smaller particles will show a large strain due to the large surface-to-volume ratio. Therefore, that strain will become weak for the TA sample as observed experimentally. Moreover, the mean crystallite size of the AP sample is very small and becomes ∼four times larger after the TA. To confirm the mean crystallite size, high resolution transmission electron microscopy (HRTEM) images were obtained for the TA sample. In order to determine the mean particle size, the particle sizes of the HRTEM images were counted using the ImageJ software. Several images were used to obtain $N = 194$ particle sizes. Subsequently, using the Sturges method a histogram distribution of particle sizes was obtained [14], which was modeled with a log-normal function (see Fig. 2). The size obtained from the HRTEM images are in good agreement with the mean crystallite size determined from XRD data analysis. Moreover, two interplanar distances were determined from the images (see Fig. 2a). By using the relation: $1/d^2 = (h^2 + k^2)/a^2 + l^2/c^2$, valid for a tetragonal structure, where h, k, l are the Miller indices and a and c are the lattice constants, the $d_1 = 0.33$ nm and $d_2 = 0.26$ nm distances have been assigned, respectively, to the (110) and (101) diffraction planes of the rutile-type structure. It is worth mentioning that these diffraction planes are commonly found in nano-sized SnO_2 systems [15].

3.2. Vibrational characterization

In Fig. 3 is shown the room temperature Raman spectra of the AP and TA samples. The peaks of the AP sample, located at 626,
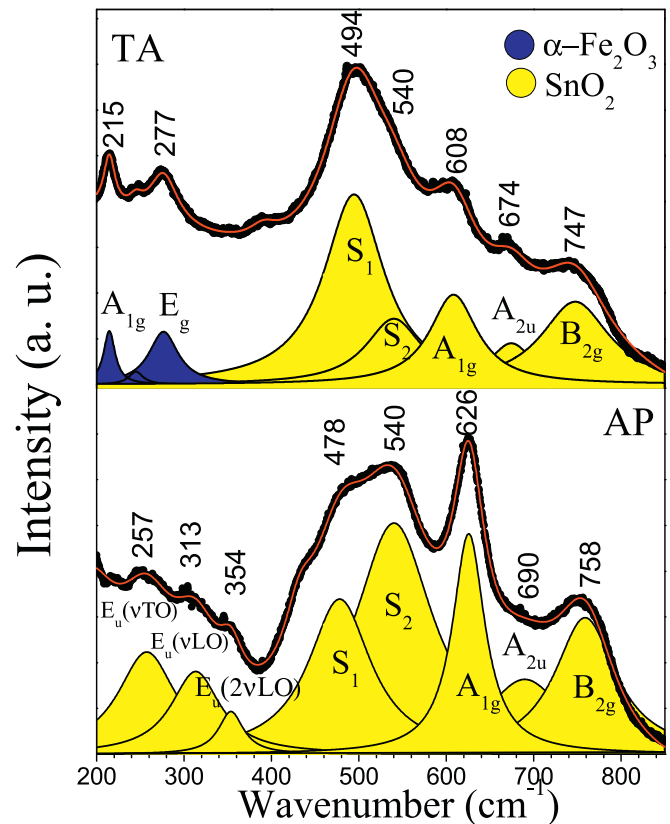
Fig. 3. Room-temperature Raman spectra of the as-prepared and thermally-annealed 10% Fe-doped SnO_2 nanoparticles. The points represent the experimental data, the line the fitting with Lorentzian peaks.
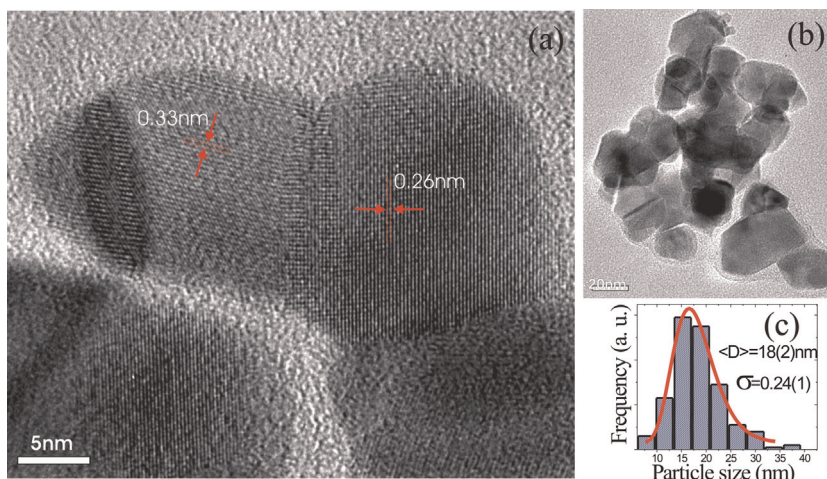
Fig. 2. (a) HRTEM of the thermally-annealed sample. The interplanar distances 0.33 and 0.26 nm are determined, which correspond to the (110) and (101) planes. b) A TEM image used to count the particle size. c) Histogram distribution of the particle size modeled with a log-normal function.

690 and 758 cm^{-1} are assigned to the A$_{1g}$, A$_{2u}$ and B$_{2g}$ vibrational modes of the rutile-type crystalline phase [18], peaks located at 257, 313 and 354 cm^{-1} are assigned to the E$_u(\nu_{TO})$, E$_u(\nu_{LO})$ and to E$_u(\nu_{2LO})$ modes, which become activated by the small particles size [19]. Bands located at 478 and 540 cm^{-1} for the as-prepared sample are attributed to the S$_1$ and S$_2$ modes, respectively, which are known as surface disorder-activated modes [18]. After the annealing, the Raman spectra shows strong modifications. The three aims modes of the rutile-type crystalline phase (A$_{1g}$, A$_{2u}$ and B$_{2g}$) experiment a redshift, with respect to the position of the AP sample. which could be explained by disorder effect originate by the out diffusion of the iron ions from the matrix caused by the thermal annealing, it worsens the crystallinity of the surface. This fact is not shown by XRD, because amorphous or poorly crystalline phase does not contribute to diffraction peaks. On the other hand, two modes located at 215 and 277 cm^{-1} emerge in the TA sample. These modes do not correspond to the rutile-type structure, but seems to correspond to the A$_{1g}$ and E$_g$ modes of hematite (α-Fe$_2$O$_3$) [19,20]. It is worth mentioning that the formation of a secondary phase is clearly detected by Raman spectroscopy and supported by the magnetic measurements discussed later on in this report. Nevertheless, the hematite phase associated to the Raman spectrum of sample TA (peaking at 215 and 277 cm^{-1}) has not been observed in the XRD data, more likely due to the limitation of the XRD system's sensitivity.

3.3. DC magnetic properties

The DC susceptibility (χ_{DC}) as a function of the temperature (T) was measured in a field H= 5 kOe for both samples. As observed in Fig. 4, the χ_{DC} vs. T curves show a typical paramagnetic behavior. No evidence of a ferromagnetic contribution is determined for the AP sample. This is in agreement with other reports [21,22], wherein a long-range ferromagnetic order that is mediated by bound magnetic polarons (BMP) is expected only for dopant levels below 1–3%. Above that dopant content, only a paramagnetic behavior is observed. The thermal dependence of the susceptibility of the AP sample could be well modeled by the Curie–Weiss law given by: $\chi_{DC} = \chi_0 + C/(T - \theta)$, where χ_0 represents any temperature-independent contribution, θ is the Curie–Weiss temperature, C is the Curie constant which is given by $C = N\mu_{eff}^2/3k_B$, N is the number of magnetic ions, μ_{eff} is the effective magnetic moment which is given by: $\mu_{eff} = 2\mu_B[S(S + 1)]^{1/2}$, where S is the spin of iron ions and μ_B is the Bohr magneton. However, the Curie–Weiss law
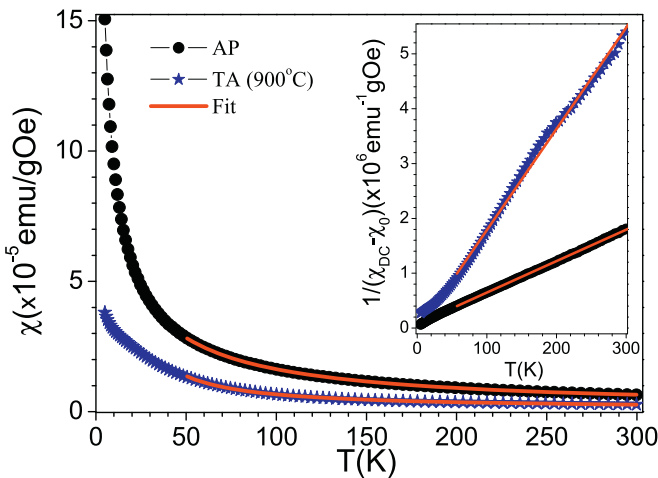
Sample	C ($\times 10^{-5}$ emu K g^{-1} Oe^{-1})	θ (K)	χ ($\times 10^{-7}$ emu g^{-1} Oe^{-1})
AP	175(1)	−13.6(2)	9.2(3)
TA	51(1)	9.8(8)	9.5(5)

is not fully satisfied for the TA sample. The broad shoulder at ∼180 K, better observed in the inset of Fig. 4, evidences the presence of other magnetic contribution. Besides that, a strong deviation from the Curie–Weiss law is observed below 50 K for the TA sample. In order to compare the results of both samples, the fits are carried out in the range from 50 to 300 K (paramagnetic region of the TA sample).

The results obtained from the analyzes are presented in Table 2. As can be observed, C decreases after the thermal annealing. The effective magnetic moment per Fe ion can be calculated from the relation: $\mu_{eff} = 2.828\sqrt{CM_m}$ (M_m is the molecular weight). We obtain 4.5 μ_B/Fe and 2.4 μ_B/Fe for the AP and TA samples, respectively. Those values are lower than the spin-only magnetic moment of the iron ion (4.90 μ_B for Fe^{2+} and 5.92 μ_B for Fe^{3+}). Since XRD data analysis suggests the occurrence of mainly Fe^{3+} ions substituting Sn^{4+} ions, the effective magnetic moments can help to estimate the percentage of iron ions (x_P) which originate the paramagnetic signal. By assuming that no short-range anti-ferromagnetic interactions occur, a $x_P \sim$6% is obtained for the as-prepared. However, due to the statistical distribution of iron ions, the probability of having Fe^{3+} with at least one nearest-neighboring Fe^{3+} which couple with each other via antiferromagnetic superexchange interaction needs to be considered. In such a case, pairs or groups of four iron ions make no net contribution, meanwhile triplets or large antiferromagnetic clusters of N iron ions will make a contribution of $\mu_{eff}/N^{1/2}$. After the thermal annealing, the paramagnetic population of magnetic ions is strongly reduced which suggests the occurrence of additional magnetic phases induced by the thermal annealing. The Raman data (see Fig. 3) support the claim for the onset of the hematite phase as a result of the annealing process, thus explaining the reduction of the paramagnetic population of the magnetic ions

Fig. 4. Temperature (T) dependence of the DC susceptibility (χ_{DC}). The inset shows the $1/(\chi_{DC} - \chi_0)$ vs. T. The points represent the experimental data and the solid lines represent the fits to the Curie–Weiss law.

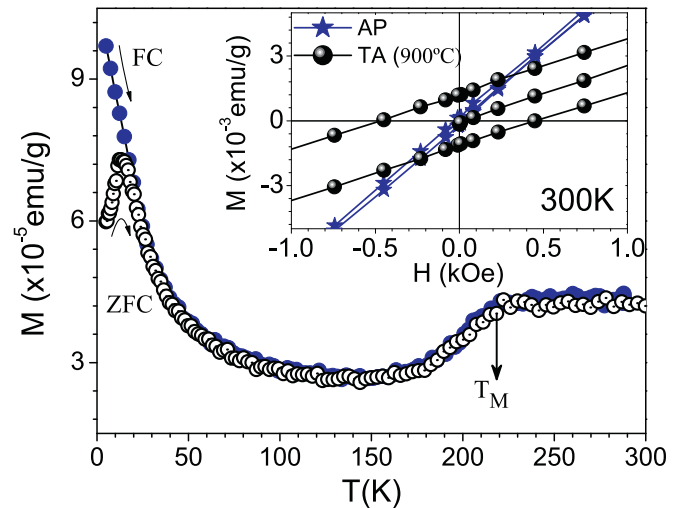**Fig. 5.** Zero-field-cooled (ZFC) and field-cooled (FC) curves for the thermally-annealed sample (H= 50 Oe). The inset shows the M vs. H curves of as-prepared and TA samples obtained at 300 K.
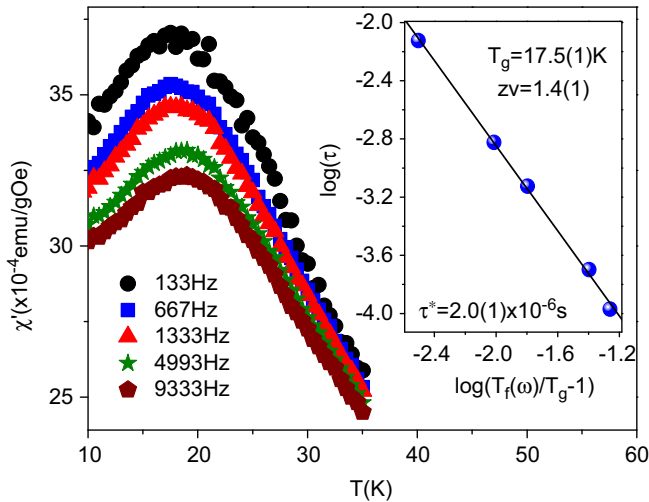
Fig. 6. Plot of the in-phase component of the AC susceptibility as function of the temperature, at different field frequencies. The inset shows the log–log plot of the critical slowing down law (Eq. 2).

observed by the Curie–Weiss law analyze. It is worth noting that the negative Curie–Weiss temperature (θ) determined for the as-prepared sample confirms the occurrence of antiferromagnetic correlations among the spins. Those correlations become ferromagnetic ($\theta > 0$) after the annealing. The reason for that signal change is not clear yet and more research is needed in order to decipher it.

Fig. 5 shows the field-cooled (FC) and zero-field-cooled (ZFC) curves obtained with a field of $H = 50$ Oe for the thermally-annealed sample. By cooling from high temperatures, the ZFC and FC curves show a sudden decrease at $T \sim 225$ K. This decrease has been assigned to a magnetic transition of the hematite (α-Fe_2O_3) phase that seems to be formed due to the segregation of the iron ions, which out-diffuse from the SnO_2 lattice. This result is in agreement with Raman spectroscopy results which show the presence of α-Fe_2O_3 phase in the TA sample. Besides that, the presence of a coercive field in the M vs. H curve for the TA sample (see inset of Fig. 5) reinforces the presence of a weak ferromagnetic contribution, associated to the hematite phase, which is not present in the as-prepared sample. It is believed that the formation of the hematite phase with a Morin transition at $T_M \sim 225$ K, seems to be favored by the thermal annealing process carried out in air (an oxidizing atmosphere). For bulk hematite, the Morin transition is expected at $T_M = 263$ K, but it is reported that this temperature decreases when the particle size decreases [23]. On the other hand, at temperatures below 150 K, the ZFC and FC curves follow the typical Curie-like behavior. Meanwhile, both curves show an irreversible behavior for temperatures below 20 K, the ZFC curve shows a maximum centered at $T \sim 14$ K. These features are commonly associated to a superparamagnetic behavior [24], cluster-glass or spin-glass systems [25].

3.4. Dynamical properties

In order to decipher the nature of the thermal relaxation features, AC magnetic measurements were carried out. In Fig. 6 is shown the curves of the real part (χ') of the AC susceptibility as a function of the temperature at different field frequencies (ω) for the TA sample. As can be observed, each χ' vs. T curves shows a maximum which position shifts to higher temperatures as ω is increased. These features are not observed for the as-prepared sample.

One can model the thermal relaxation of the magnetic moments by the Arrhenius law: $\tau = \tau_0 \exp(E_a/k_B T)$, where $\tau = 1/\omega$, τ_0 is a characteristic time (usual values are in the range of 10^{-9}–10^{-13} s), E_a is the energy barrier which separates two different low-energy states. Assuming that the maximum of the χ' vs. T curve represents the freezing temperature, $T_f(\omega)$, the plot of $ln(\tau)$ vs. $1/T_f(\omega)$ shows a linear behavior. From the linear fit an $E_a/k_B = 1356 K$ and $\tau_0 \approx 10^{-36} s$ are determined. The value of τ_0 is physically unacceptable which excludes the possibility of having a non-interacting superparamagnetic system and suggests that the frequency dependence of T_f could describe a spin-glass behavior which seems to appear only after the thermal annealing process. Moreover, the calculation of the empirical parameter: $\Phi = \Delta T_f/T_f \Delta \log_{10}(\omega)$, where $\Delta T_f/T_f$ is the relative variation of the freezing temperature and $\Delta \log_{10}(\omega)$ is the frequency decade variation, provides a value of $\Phi = 0.031$. Usual values collected from the literature are in the range of $\Phi \sim 0.005$–0.01 for canonical spin glasses, $\Phi \sim 0.03$–0.06 for cluster-glass systems, and $\Phi > 0.1$ for superparamagnetic systems [26,27].

The existence of a true spin-glass phase transition implies that the relaxation time of magnetic entities shows a critical behavior below the transition temperature, T_g. The description of this critical phenomenon is usually ruled by the critical slowing down law given by [28]:

$$\tau = \tau^* \left[T_f(\omega)/T_g - 1 \right]^{-z\nu} \tag{2}$$

Where z the dynamic critical exponent, ν is the critical exponent describing the divergent behavior of the correlation length (ξ) and τ^* is a microscopic relaxation time. The existence of a true phase transition can be tested using the cusp position of the χ' vs. T curves. A good linearity is obtained in the log–log plot as showed in the inset of Fig. 6 and the linear fit provides a $T_g = 17.5(1)$ K, $z\nu = 1.4(2)$ and $\tau^* = 2.0(2) \times 10^{-6}$ s. Although a small value of $z\nu$ has been determined, it is consistent with some reported values for cluster-glass (CG) systems ($z\nu \sim 3$) [29]. The τ^* is much larger than the typical values of conventional spin glass systems ($\tau^* \sim 10^{-13}$ s) and near to values reported for CG systems ($\tau^* \sim 10^{-7}$–10^{-9} s) [30]. Based on the experimental results, we speculate that this cluster-glass behavior could arise from magnetic clusters formed at the particle surface due to the segregated iron ions caused by the annealing process. Due to the topological disorder, those clusters could randomly interact with each other and provide the adequate scenario to show magnetic frustrations.

4. Conclusions

10% Fe-doped SnO_2 nanoparticles were successfully synthesized by a polymeric precursor method. XRD data analyzes show the formation of tetragonal rutile-type structure in the as prepared and thermally-treated samples. The analysis of the χ_{DC} vs. T curve indicates a paramagnetic behavior for the as-prepared sample. After annealing, the coexistence of a paramagnetism and magnetically ordered contribution, which has been assigned to the formation of an iron oxide (likely α-Fe_2O_3) phase induced, is determined. The thermal relaxation features observed in DC and AC susceptibility measurements for the thermally-treated sample have been assigned to the formation of clusters of spins likely at the particle surface which show a cluster-glass behavior. These spin clusters seem to be formed due to the out diffusion of iron ions from the core of the SnO_2 matrix caused by the annealing process.

Acknowledgments

References

[1] A. Punnoose, K.M. Reddy, J. Hays, A. Thurber, M.H. Engelhard, Appl. Phys. Lett. 89 (2006) 112509.
[2] A. Thurber, K.M. Reddy, A. Punnoose, J. Appl. Phys. 105 (2009) 07E706.
[3] B. Bahrami, A. Khodadadi, M. Kazemeini, Y. Mortazavi, Sens. Actuators B 133 (2008) 352.
[4] R. Pearce, W.R. Patterson, Catalysis and Chemical Processes, Leonard Hill, Glasgow, 1981.
[5] K.G. Godinho, A. Walsh, G.W. Watson, J. Phys. Chem. C 113 (2009) 439.
[6] P. Hidalgo, R.H.R. Castro, A.C.V. Coelho, D. Gouvêa, Chem. Mater. 17 (2005) 4149.
[7] A. Punnoose, J. Hays, A. Thurber, M.H. Engelhard, R.K. Kukkadapu, C. Wang, V. Shutthanandan, S. Thevuthasan, Phys. Rev. B 72 (2005) 054402.
[8] X. Mathew, C. Mejía-García, G. Contreras-Puente, A. Punnoose, J. Appl. Phys. 99 (2006) 08M101.
[9] R. Adhikari, A.K. Das, D. Karmakar, T.V. Chandrasekhar Rao, J. Ghatak, Phys. Rev. B 78 (2008) 024404.
[10] J. Okabayashi, S. Kono, Y. Yamada, K. Nomura, J. Appl. Phys. 112 (2012) 073917.
[11] R.H.R. Castro, P. Hidalgo, R. Muccillo, D. Gouvêa, Appl. Surf. Sci. 214 (2003) 172.
[12] R.A. Young, Allen C. Larson, C.O. Paiva-Santos, User's Guide to Program DBWS-9411 for Rietveld Analysis of X-ray and Neutron Powder Diffraction Patterns, Atlanta (1994).
[13] C. Paiva-Santos, A. Cavalheiro, M.A. Cilense, J.A. Varela, M. Silva, Y. Mascarenhas, Adv. X-ray Anal. 44 (2001) 38.
[14] F.H. Aragón, P.E.N. de Souza, J.A.H. Coaquira, P. Hidalgo, D. Gouvêa, Physica B 407 (2012) 2601.
[15] E.J.H. Lee, C. Ribeiro, T.R. Giraldi, E. Longo, E.R. Leite, Appl. Phys. Lett. 84 (2004) 1745.
[16] F.H. Aragón, R. Cohen, J.A.H. Coaquira, G.V. Barros, P. Hidalgo, L.C.C. M. Nagamine, D. Gouvêa, Hyperfine Intereact. 202 (2011) 73.
[17] W.H. Baur, A.A. Khan, Acta Crystallogr. B27 (1971) 2133.
[18] F.H. Aragón, J.A.H. Coaquira, P. Hidalgo, S.W. da Silva, S.L.M. Brito, D. Gouvêa, P. C. Morais, J. Raman Spectrosc. 42 (2010) 1081.
[19] J.J. Beltran, L.C. Sánchez, J. Osorio, L. Tirado, E.M. Baggio-Saitovitch, C. A. Barrero, J. Mater. Sci. 45 (2010) 5002.
[20] F. Nakagomi, S.W. da Silva, V.K. Garg, A.C. Oliveira, P.C. Morais, A. Franco Júnior, E.C.D. Lima, J. Appl. Phys. 101 (2007) 09M514.
[21] F.H. Aragón, V.A. Chitta, J.A.H. Coaquira, P. Hidalgo, H.F. Brito, J. Appl. Phys. 114 (2013) 203902.
[22] F.H. Aragón, J.A.H. Coaquira, P. Hidalgo, S.L.M. Brito, D. Gouvêa, R.H.R. Castro, J. Phys.: Condens. Matter 22 (2010) 496003.
[23] R.D. Zysler, D. Fiorani, A.M. Testa, L. Suber, E. Agostinelli, M. Godinho, Phys. Rev. B 68 (2003) 212408.
[24] G.F. Goya, T.S. Berquo, F.C. Fonseca, M.P. Morales, J. Appl. Phys. 94 (2003) 3520.
[25] A. Labarta, X. Batlle, B. Martínez, X. Obradors, Phys. Rev. B 46 (1992) 8994.
[26] J.A. Mydosh, Spin glasses: An Experimental Introduction, Taylor & Francis, London, 1993.
[27] R. Mahendiran, Y. Breard, M. Hervieu, B. Raveau, P. Schiffer, Phys. Rev. B 68 (2003) 104402.
[28] Spin Glasses and Random Fields, Series on Directions in, in: A.P. Young (Ed.), Condensed Matter Physics, vol. 12, World Scientific, Singapore, 1998.
[29] S. Mukherjee, R. Ranganathan, Phys. Rev. B 54 (1996) 9267.
[30] M.H. Phan, N.A. Frey, H. Srikanth, M. Angst, B.C. Sales, D. Mandrus, J. Appl. Phys. 105 (2009) 07E308.